

Theoretical period–radius and period–luminosity relations for Mira variables with solar metallicity

Yu. A. Fadeyev*

*Institute of Astronomy, Russian Academy of Sciences, Pyatnitskaya ul. 48, Moscow, 119017
Russia*

Received October 16, 2023; revised November 6, 2023; accepted November 6, 2023

Abstract — Evolutionary sequences of AGB stars with initial masses on the main sequence $M_{\text{ZAMS}} = 1.5M_{\odot}$, $2M_{\odot}$ and $3M_{\odot}$ were computed for the initial metallicity $Z = 0.014$. Selected models of evolutionary sequences with envelopes under thermal equilibrium were used as initial conditions for calculation of nonlinear stellar pulsations. The hydrodynamic models of each evolutionary sequence are shown to concentrate along the continuous line in the period–radius and period–luminosity diagrams. The theoretical period–radius and period–luminosity relations differ from one another for different main–sequence star masses because the stellar luminosity of AGB stars depends on the degenerate carbon core mass which increases with increasing M_{ZAMS} . In hydrodynamic models of evolutionary sequences $M_{\text{ZAMS}} = 2M_{\odot}$ and $M_{\text{ZAMS}} = 3M_{\odot}$ the periods of the first overtone pulsators are $86 \text{ d} \leq \Pi \leq 123 \text{ d}$ and $174 \text{ d} \leq \Pi \leq 204 \text{ d}$, whereas all models of the evolutionary sequence $M_{\text{ZAMS}} = 1.5M_{\odot}$ oscillate in the fundamental mode. Fairly regular radial oscillations exist in stars with pulsation periods $\Pi \lesssim 500 \text{ d}$. In models with longer periods the amplitude rapidly increases with increasing Π and oscillations become irregular.

Keywords: *stellar evolution; stellar pulsation; stars: variable and peculiar*

*E-mail: fadeyev@inasan.ru

INTRODUCTION

Soon after the discovery of a correlation between the period of light variations and the bolometric magnitude in eleven Mira pulsating variables of the Large Magellanic Cloud (Glass and Lloyd Evans 1981) these stars became a reliable distance indicator together with the classical Cepheids (Glass and Feast 1982a; 1982b; Feast 1985). The near-infrared radiation at wavelengths $\sim 2 \mu\text{m}$ is less sensitive to the interstellar extinction in comparison with the optical range and due to the large luminosity in the infrared the distance scale of Miras extends much further in comparison with that of Cepheids. Moreover, more reliable estimates of bolometric magnitudes provided by the near-infrared photometry play an important role in comparison of theoretical models with observations of Mira variables.

The period–luminosity relation was first determined from observations of Mira variables in the Magellanic Clouds (Feast 1984; Feast et al. 1989; Groenewegen and Whitelock 1996). Somewhat later the similar correlations between the luminosity and the period of light variations were found for Miras observed in galaxies of the Local Group M31 (Mould et al. 2004), M33 (Mould et al. 1990; Yuan et al. 2018), NGC 4528 (Huang et al. 2018) and NGC 6822 (Whitelock et al. 2013). The period–luminosity relation of galactic Miras is based on measurements of their trigonometric parallaxes obtained with the VLBI observations (Chibueze et al. 2020; Urago et al. 2020; Sun et al. 2022) as well as with astrometric satellites Hipparcos (Whitelock et al. 2000; Whitelock and Feast 2000) and Gaia (Andriantsaralaza et al. 2022; Zhang and Sanders 2023).

It is intuitively clear that the existence of the period–luminosity relation of Miras is due to the evolution of AGB stars of various masses, ages and composition. Therefore, the nature of this relationship can only be understood with the help of consistent stellar evolution and stellar pulsation computations. Unfortunately, no detailed consistent computations have been done so far in this field. The purpose of this work is to fill this gap for the AGB stars with a solar metallicity. Below we present the results of the Cauchy problem solution for the equations of radiation hydrodynamics describing the nonlinear stellar pulsations and where the selected AGB stellar evolution models are used as the initial conditions. The final goal of hydrodynamic calculations is to determine the mean pulsation period Π of the hydrodynamic model after attainment of the limiting amplitude when Π is time-independent.

EVOLUTIONARY SEQUENCES OF AGB STARS

In this work we considered the evolution of stars with masses on the main sequence $M_{\text{ZAMS}} = 1.5M_{\odot}$, $2M_{\odot}$ and $3M_{\odot}$. The initial abundance of helium was set to be $Y = 0.28$ whereas the abundance of heavier elements was assumed to correspond to the solar metallicity $Z = 0.014$

(Asplund et al. 2009). Calculations of the stellar evolution from the main sequence up to the final AGB stage were done with the program MESA version r15140 (Paxton et al. 2019). Convective mixing of the stellar matter was treated via the theory of Böhm–Vitense (1958) for the mixing length to pressure scale height ratio $\alpha_{\text{MLT}} = 1.8$. Extra mixing due to overshooting at the convection zone boundaries was calculated according to Herwig (2000) and Pignatari et al. (2016). The nuclear energy generation rates and the nucleosynthesis were calculated with the help of the JINA Reaclib database (Cyburt et al. 2010). The mass loss rate due to the stellar wind was calculated according to Reimers (1975) with the parameter $\eta_{\text{R}} = 0.5$ at evolutionary stages prior to the AGB whereas at the AGB phase the mass loss rate was computed using the formula of Bloeker (1995) with the parameter $\eta_{\text{B}} = 0.05$. To evaluate the role of uncertainties in the mass loss rates we computed two additional evolutionary sequences $M_{\text{ZAMS}} = 1.5M_{\odot}$ and $3M_{\odot}$ with the mass loss rate parameter $\eta_{\text{B}} = 0.03$.

The theory of stellar pulsation is only applicable to models of stellar envelopes under both the hydrostatic and thermal equilibrium. The first of these conditions is always fulfilled since the solution of the equations of stellar evolution describes the stellar structure under the hydrostatic equilibrium. However at some evolutionary stages the stellar envelope is in thermal imbalance owing to changes of its gravitational energy during envelope contraction or expansion.

The equation of energy conservation for the spherically–symmetric star is

$$\frac{dL_r}{dM_r} = \varepsilon - \varepsilon_{\nu} - T \frac{\partial S}{\partial t}, \quad (1)$$

where M_r is the Lagrangean coordinate which equals the mass confined to a radius r , L_r is the total (radiative plus convective) luminosity in the layer with radius r , ε is the nuclear energy generation rate, ε_{ν} is the cooling rate via neutrino emission, T and S are the temperature and specific entropy of the stellar matter, t is time. Analysis of stellar pulsation is usually restricted to outer layers of the red giant with temperature $T \lesssim 10^7$ K so that the first two terms on the right–hand side of (1) are negligible and can be omitted. Therefore, the condition of the thermal equilibrium in the spherically–symmetric stellar envelope is written as

$$\frac{dL_r}{dM_r} = 0. \quad (2)$$

In the present study to measure the deviation from thermal equilibrium we used the parameter

$$\delta_{\text{L}} = \max_{1 \leq j \leq N} |1 - L_j/L_0|, \quad (3)$$

where L_j is the total luminosity at the j –th Lagrangean zone, $j = 0$ and $j = N$ correspond to the inner and outer boundaries of the stellar envelope model. Earlier we have shown (Fadeyev 2022) that the condition $\delta_{\text{L}} \lesssim 10^{-2}$ is a good approximation of the thermal equilibrium in the stellar model.

Fig. 1 shows variations of the stellar radius R and parameter δ_L for the evolutionary sequence $M_{\text{ZAMS}} = 2M_{\odot}$ during the time intervals comprising the fifth ($i_{\text{TP}} = 5$) and the sixth ($i_{\text{TP}} = 6$) thermal helium–shell flashes. For the sake of convenience, the evolution time t_{ev} is set to zero at the peak helium shell luminosity $L_{3\alpha}$ for $i_{\text{TP}} = 5$ when the stellar mass is $M = 1.97M_{\odot}$. The deviation from thermal equilibrium was calculated for the stellar envelope with the inner boundary at the Lagrangean coordinate $M_r = 0.526M_{\odot}$. Within the time interval shown in Fig. 1 the radius and temperature of the envelope inner boundary varies within $0.073R_{\odot} \leq r_0 \leq 4.66R_{\odot}$ and $6.1 \times 10^5 \text{ K} \leq T_0 \leq 2.3 \times 10^7 \text{ K}$, respectively. As seen in Fig. 1, the stellar envelope is in thermal imbalance (i.e. $\delta_L > 0.01$) during $\approx 1.4 \times 10^4 \text{ yr}$ or $\approx 10\%$ of the interflash period. Thus, the models in thermal equilibrium allow us to reproduce the period–luminosity dependence with a sufficiently good accuracy for $\approx 90\%$ of Mira lifetime.

HYDRODYNAMIC MODELS OF MIRAS

Hydrodynamic models of pulsating AGB stars are computed via solution of the Cauchy problem for equations of radiation hydrodynamics describing the spherically–symmetric motions of the stellar envelope. The convective luminosity and the flux of the mean specific turbulent energy are calculated with the help of the transport equations for the time–dependent turbulent convection (Kuhfuß 1986). The general system of the equations of hydrodynamics and parameters of the convection theory are discussed in our earlier paper (Fadeyev 2013).

The initial conditions for the Cauchy problem were computed for selected evolutionary models with deviation from thermal equilibrium in the outer convection zone $\delta_L < 10^{-2}$. The inner boundary of the hydrodynamic model was set in layers with the temperature $10^6 \text{ K} \lesssim T \lesssim 10^7 \text{ K}$ and radius $r_0 \lesssim 10^{-3}R$, where R is the radius of the outer boundary of the evolutionary model. The Lagrangean grid of the hydrodynamic model is computed for mass intervals ΔM_r increasing geometrically inward. Significant difficulties in the hydrodynamic calculations of Mira models appear because of sharply increasing pressure and temperature gradients in the layers with temperature $T \gtrsim 10^6 \text{ K}$. To avoid the large approximation errors at the bottom of the convection zone we used the Lagrangean grid with 100 innermost mass intervals decreasing geometrically inwards. The boundary between the regions with increasing and decreasing mass intervals locates in layers with temperature $T \sim 10^5 \text{ K}$.

Evolutionary computations of AGB star models were done with the number of mass zones $3 \times 10^3 \lesssim N_{\text{MESA}} \lesssim 5 \times 10^3$ whereas the number of mass zones in the hydrodynamic models of stellar envelopes was in the range $600 \leq N \leq 900$. The larger number of mass zones was used in pulsation calculations of late AGB stars because of their high amplitude oscillations. Initial values of the variables at the grid nodes were calculated using the nonlinear interpolation of the evolutionary model data with respect to Lagrangean coordinate M_r .

The solution of the Cauchy problem describes the self-excited stellar oscillations where the role of small initial perturbations is played by interpolation errors accompanying the calculation of initial conditions. The plots illustrating the amplitude growth with subsequent limiting amplitude attainment are shown in Figs. 2 and 3 for two hydrodynamic models of the evolutionary sequence $M_{\text{ZAMS}} = 2M_{\odot}$. For the sake of graphical convenience the results of hydrodynamic computations are illustrated by the plots of the maximum values of the kinetic energy of pulsation motions $E_{\text{K,max}}$ as well as by the maximum and minimum values of the outer boundary radius R_{max} and R_{min} .

Both models shown in Figs. 2 and 3 are characterized by high amplitude growth rates whereas the limiting amplitude attainment is not only due to saturation of the κ -mechanism responsible for excitation of oscillations, but also due to abrupt dissipation of the kinetic energy by shock waves appearing in the outer layers of the hydrodynamic model. Different amplitude growth rates ($\eta = \Pi d \ln E_{\text{K,max}}/dt = 0.032$ for the model in Fig. 2 and $\eta = 0.42$ for the model in Fig. 3) are due to extension of the hydrogen ionizing zone and increasing pulsation instability as a star evolves along the AGB.

The most striking feature of the plots in Figs. 2 and 3 is variations of the kinetic energy and radius of the outer boundary after the cessation of the instability growth. In the first case (see Fig. 2) the solution converges to fairly regular oscillations with nearly constant amplitude whereas in the second case (see Fig. 3) the regular oscillations are not attained because of the large amplitude of the outer layers even despite significantly longer integration with respect to time.

The mean stellar radius after the cessation of the instability growth \bar{R} was evaluated with the help of the discrete Fourier transform and as is seen in Figs. 2 and 3, the estimates of \bar{R} noticeably exceed the equilibrium stellar radius R_{eq} . The difference between \bar{R} and R_{eq} is due to the large amplitude oscillations and periodic shock waves that lead to distension of the outer stellar envelope (Willson 2000). In the model shown in Fig. 2 the ratio of the mean radius to the equilibrium radius is $\bar{R}/R_{\text{eq}} = 1.07$ whereas the mean amplitude of the radial displacement at the outer boundary is $\Delta R/\bar{R} = 0.52$. In the model shown in Fig. 3 these quantities are $\bar{R}/R_{\text{eq}} = 1.21$ и $\Delta R/\bar{R} = 0.65$.

The mean pulsation period was calculated with the help of the discrete Fourier transform of the kinetic energy of pulsation motions after attainment of limiting amplitude. The method of period evaluation is illustrated in Fig. 4 where the plots of the spectral density of the kinetic energy $S_{\nu}(E_{\text{K}})$ in the vicinity of the main oscillation frequency are shown for two hydrodynamic models with different behavior of limiting amplitude oscillations. The plot in Fig. 4a corresponds to the hydrodynamic model shown in Fig. 2 and the period is easily determined from the maximum of $S_{\nu}(E_{\text{K}})$. The plot of the spectral density in Fig. 4b corresponds to irreg-

ular oscillations and the mean period is evaluated from the maximum of the Gaussian function fitting the spectrum $S_\nu(E_K)$ using the least-squares method.

To obtain the reliable estimates of the mean pulsation period Π we carried out the calculations of stellar pulsations on the intervals comprising more than 10^3 periods. However one should bear in mind that the cessation of amplitude growth does not necessarily imply that the model reaches the limiting amplitude oscillations because cessation of the amplitude growth is usually followed by the model relaxation with slowly changing mean values of \bar{R} and luminosity \bar{L} . Results of preliminary calculations allow us to conclude that a criterion of limiting amplitude oscillations is $\bar{L} = L_0$, where L_0 is the total luminosity at the inner boundary of the hydrodynamic model. In the present study the calculations of hydrodynamic models were ended as soon as the time interval of the discrete Fourier transform reaches $t/\Pi \approx 10^3$ and the difference between L_0 and the mean luminosity \bar{L} does not exceed 0.1%.

PERIOD–RADIUS AND PERIOD–LUMINOSITY RELATIONS

In this work we computed 150 hydrodynamic models of Mira variables. Nearly 30 models were found to be stable against radial oscillations since they showed the decaying amplitude. The period–radius $\Pi - \bar{R}$ and period–luminosity $\Pi - \bar{L}$ dependencies determined with the help of hydrodynamic models are shown in Figs. 5 and 6 for pulsations in the fundamental mode and first overtone, respectively.

As mentioned above, the evolutionary sequences $M_{\text{ZAMS}} = 1.5M_\odot$ and $3M_\odot$ were computed with the mass loss rate parameters $\eta_B = 0.03$ and $\eta_B = 0.05$. In Figs. 5 and 6 the corresponding hydrodynamic models are shown by the triangles and circles. It is seen that the models of each evolutionary sequence are concentrated along the continuous line and are almost independent of η_B .

The dashed lines in Figs. 5 and 6 represent the linear least-squares fits

$$\lg \bar{R}/R_\odot = a_0 + a_1 \lg \Pi_k, \quad (4)$$

$$\lg \bar{L}/L_\odot = b_0 + b_1 \lg \Pi_k, \quad (5)$$

where $k = 0$ and $k = 1$ correspond to the fundamental mode and first overtone pulsations, respectively. The coefficients a_0, a_1, b_0, b_1 in (4) and (5) as well as the ranges of corresponding period intervals (Π_a, Π_b) are listed in Table 1.

As seen in Fig. 5, the scatter of points becomes larger with increasing Π and indicates an increase in errors of the pulsation period estimates for $\Pi > 500$ d. Moreover, the models with longest periods show the systematic deviations in the period–luminosity diagram to smaller values of \bar{L} though the similar deviations in the period–radius diagram are not present.

The systematic deviations in Fig. 5b are due to the strong non-linearity of long period stellar pulsations. On the other hand, the systematic deviations in the period–radius diagram are not present because the increase of non-linearity is accompanied by increase both in period and radius because they relate as $\Pi \propto \bar{R}^{3/2}$. Similar transformations in the $\Pi - \bar{L}$ diagram are impossible because the mean stellar luminosity remains constant so that increase of stellar pulsation period with increasing pulsation amplitude leads to the shift along the horizontal axis of the diagram.

In the present study the period–radius and period–luminosity relations were determined for the models of evolutionary sequences $M_{\text{ZAMS}} = 1.5M_{\odot}$, $2M_{\odot}$ and $3M_{\odot}$ pulsating in the fundamental mode and first overtone within the whole period interval. The only exception is the period–luminosity relation for the fundamental mode pulsators where the period interval is limited to the linear dependence between $\log \Pi$ and $\log \bar{L}$.

CONCLUSION

The theoretical period–radius and period–luminosity relations for Mira models with solar metallicity were determined on the basis of consistent calculations of stellar evolution nonlinear stellar pulsations. This method is applicable for the stellar envelopes under thermal equilibrium and allows us to consider $\approx 90\%$ of these stars. Results of computations show that the theoretical period–radius and period–luminosity relations depend on the initial mass of the star on the main sequence. For example, the fundamental mode oscillations with period $\Pi = 400$ d appear in models of evolutionary sequences $M_{\text{ZAMS}} = 1.5M_{\odot}$ and $M_{\text{ZAMS}} = 3M_{\odot}$ with the luminosity difference $\Delta m_{\text{bol}} \approx 0.7$ mag. Dependence of $\Pi - \bar{R}$ and $\Pi - \bar{L}$ on M_{ZAMS} is due to the fact that the total luminosity of AGB stars is a function of the mass of the degenerate carbon core and monotonically increases with increasing core mass (Paczynski, 1970; Uus 1970). Therefore, the dispersion of the observable relations $\Pi - R$ and $\Pi - L$ is not only due to observational errors but also due to different initial masses of observed stars. It is also clear that the relations $\Pi - \bar{R}$ and $\Pi - \bar{L}$ computed for the mass loss rate parameters $\eta_{\text{B}} = 0.03$ and $\eta_{\text{B}} = 0.05$ insignificantly differ from one another. Indeed, the pulsation period and stellar mass relate as $\Pi \propto M^{-1/2}$ and therefore decrease in stellar mass during the initial AGB phase does not affect the pulsation period and plays a perceptible role only during the short final AGB stage.

It is noteworthy to mention that the periods of the first overtone pulsators range in rather narrow intervals: $86 \text{ d} \leq \Pi \leq 123 \text{ d}$ and $174 \text{ d} \leq \Pi \leq 204 \text{ d}$ for $M_{\text{ZAMS}} = 2M_{\odot}$ and $M_{\text{ZAMS}} = 3M_{\odot}$, respectively. More dense grids of evolutionary sequences and hydrodynamic models will probably help to identify the pulsation modes of Mira variables.

The main difficulties in hydrodynamic modeling of Mira variables arise in computations of late AGB star models when the large oscillation amplitude leads to bad convergence of

iterative solution of implicit difference equations. A method for overcoming this obstacle implies enlargement of the number of Lagrangean zones in the hydrodynamic model with simultaneous reduction of the integration time step. Unfortunately, this approach leads to a significant increase in computational time. Moreover, the problem becomes more difficult because in order to obtain a reliable estimate of the period of large amplitude oscillations the equations of hydrodynamics should be solved on the longer time interval.

More severe difficulties arise in computation of Mira hydrodynamic models with periods $\Pi \sim 10^3$ d corresponding to the final evolutionary phase of AGB. In the present study we failed to obtain the stable solution of the equations of hydrodynamics because even small computational errors lead to the dynamical instability and expansion of the outer Lagrangean zones with velocity exceeding the local escape velocity. The problem is that the envelope of the late-phase AGB star is near the boundary of dynamical instability because of the widely extended hydrogen ionizing zone where the adiabatic exponent is below its critical value ($\Gamma_1 = (\partial \ln P / \partial \ln \rho)_S < 4/3$) whereas the surface gravity becomes too low due to the large stellar radius. A similar opinion has been earlier expressed by Tuchman et al. (1978; 1979) in their discussion of non-linear stellar pulsation as the cause of planetary nebula formation.

REFERENCES

1. M. Andriantsaralaza, S. Ramstedt, W.H.T. Vlemmings, and E. De Beck, *Astron. Astrophys.* **667**, A74 (2022).
2. M. Asplund, N. Grevesse, A.J. Sauval and P. Scott, *Ann. Rev. Astron. Astrophys.* **47**, 481 (2009).
3. T. Blöcker, *Astron. Astrophys.* **297**, 727 (1995).
4. E. Böhm–Vitense, *Zeitschrift für Astrophys.* **46**, 108 (1958).
5. J.O. Chibueze, R. Urago, T. Omodaka, Yu. Morikawa, M.Y. Fujimoto, A. Nakagawa, T. Nagayama, T. Nagayama, and K. Hirano, *Publ. Astron. Soc. Japan* **72**, 59 (2020).
6. R.H. Cyburt, A.M. Amthor, R. Ferguson, Z. Meisel, K. Smith, S. Warren, A. Heger, R.D. Hoffman, T. Rauscher, A. Sakharuk, H. Schatz, F.K. Thielemann, and M. Wiescher, *Astrophys. J. Suppl. Ser.* **189**, 240 (2010).
7. Yu.A. Fadeyev, *Astron. Lett.* **39**, 306 (2013).
8. Yu.A. Fadeyev, *MNRAS* **514**, 5996 (2022).
9. M.W. Feast, *MNRAS* **211**, 51 (1984).
10. M.W. Feast, *Observatory* **105**, 85 (1985)
11. M.W. Feast, I.S. Glass, P.A. Whitelock and R.M. Catchpole, *MNRAS* **241**, 375 (1989).
12. I.S. Glass and T. Lloyd Evans, *Nature* **291**, 303 (1981).
13. I.S. Glass and M.W. Feast, *MNRAS* **198**, 199 (1982a).
14. I.S. Glass and M.W. Feast, *MNRAS* **199**, 245 (1982b).
15. M.A.T. Groenewegen and P.A. Whitelock, *MNRAS* **281**, 1347 (1996).
16. F. Herwig, *Astron. Astrophys.* **360**, 952 (2000).
17. C.D. Huang, A.G. Riess, S.L. Hoffmann, Ch. Klein, J. Bloom, W. Yuan, M. M. Lucas, D.O. Jones, P.A. Whitelock, S. Casertano, and R.I. Anderson, *Astrophys. J.* **857**, 67 (2018).
18. R. Kuhfuß, *Astron. Astrophys.* **160**, 116 (1986).

19. J. Mould, J.R. Graham, K. Matthews Keith, G. Neugebauer, and J. Elias, *Astrophys. J.* **349**, 503 (1990).
20. J. Mould, A. Saha Abhijit, and S. Hughes, *Astrophys. J. Suppl. Ser.* **154**, 623 (2004).
21. B. Paczyński, *Acta Astron.* **20**, 47 (1970).
22. B. Paxton, R. Smolec, J. Schwab, A. Gaulty, L. Bildsten, M. Cantiello, A. Dotter, R. Farmer, J.A. Goldberg, A.S. Jermyn, S.M. Kanbur, P. Marchant, A. Thoul, R.H.D. Townsend, W.M. Wolf, M. Zhang, and F.X. Timmes, *Astrophys. J. Suppl. Ser.* **243**, 10 (2019).
23. M. Pignatari, F. Herwig, R. Hirschi, M. Bennett, G. Rockefeller, C. Fryer, F.X. Timmes, C. Ritter, A. Heger, S. Jones, U. Battino, A. Dotter, R. Trappitsch, S. Diehl, U. Frischknecht, A. Hungerford, G. Magkotsios, C. Travaglio, and P. Young, *Astrophys. J. Suppl. Ser.* **225**, 24 (2016).
24. D. Reimers, *Problems in stellar atmospheres and envelopes* (Ed. B. Baschek, W.H. Kegel, G. Traving, New York: Springer-Verlag, 1975), p. 229.
25. Y. Sun, B. Zhang, M.J. Reid, Sh. Xu, Sh. Wen, J. Zhang, and X. Zheng, *Astrophys. J.* **931**, 74 (2022).
26. Y. Tuchman, N. Sack, and Z. Barkat, *Astrophys. J.* **219**, 183 (1978).
27. Y. Tuchman, N. Sack, and Z. Barkat, *Astrophys. J.* **234**, 217 (1979).
28. R. Urigo, R. Yamaguchi, T. Omodaka, T. Nagayama, J.O. Chibueze, M.Y. Fujimoto, T. Nagayama, A. Nakagawa, Yu. Ueno, M. Kawabata, T. Nakaoka, K. Takagi, M. Yamanaka, K. Kawabata, *Publ. Astron. Soc. Japan* **72**, 57 (2020).
29. U. Uus, *Nauchn. Inform. Astron. Sovet AN SSSR* **17**, 25 (1970).
30. P.A. Whitelock and M.W. Feast, *MNRAS* **319**, 759 (2000).
31. P.A. Whitelock, F. Marang Freddy and M.W. Feast, *MNRAS* **319**, 728 (2000).
32. P.A. Whitelock, J.W. Menzies, M.W. Feast, F. Nsengiyumva, and N. Matsunaga, *MNRAS* **428**, 2216 (2013).
33. L.A. Willson, *Annual Rev. Astron. Astrophys* **38**, 573 (2000).
34. W. Yuan, M.M. Lucas, A. Javadi, Zh. Lin, and J.Z. Huang, *Astron. J.* **156**, 112 (2018).
35. H. Zhang and J.L. Sanders, *MNRAS* **521**, 1462 (2023).

Table 1. Parameters of the period–radius (4) and period–luminosity (5) relations.

$M_{\text{ZAMS}}/M_{\odot}$	k	a_0	a_1	Π_a	Π_b	b_0	b_1	Π_a	Π_b
1.5	0	1.051	0.558	116	245	1.962	0.689	116	245
2.0	0	1.110	0.554	137	309	2.009	0.723	137	244
	1	1.003	0.681	86	123	1.709	0.964	86	123
3.0	0	1.183	0.547	204	397	2.196	0.709	204	330
	1	1.237	0.600	174	204	2.451	0.698	174	204

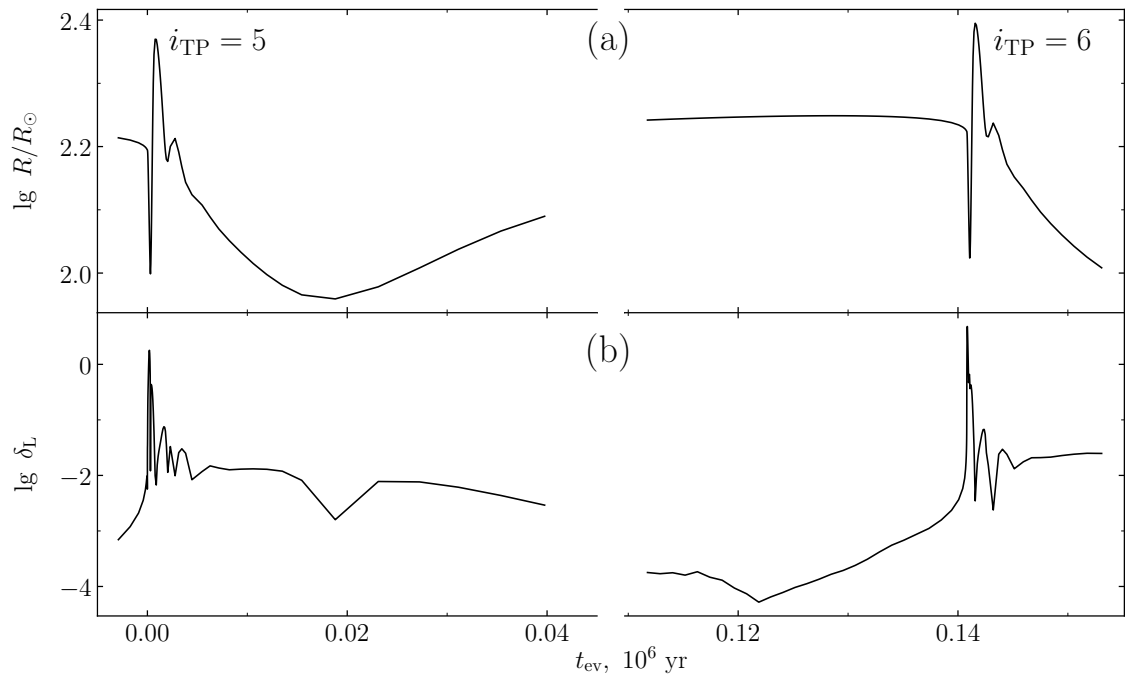


Figure 1. The time dependence of radius of the evolutionary model (a) and deviation from thermal equilibrium (b) in the convection zone of the star with initial mass $M_{\text{ZAMS}} = 2M_{\odot}$ during the time intervals comprising the 5-th and 6-th thermal helium-shell flashes.

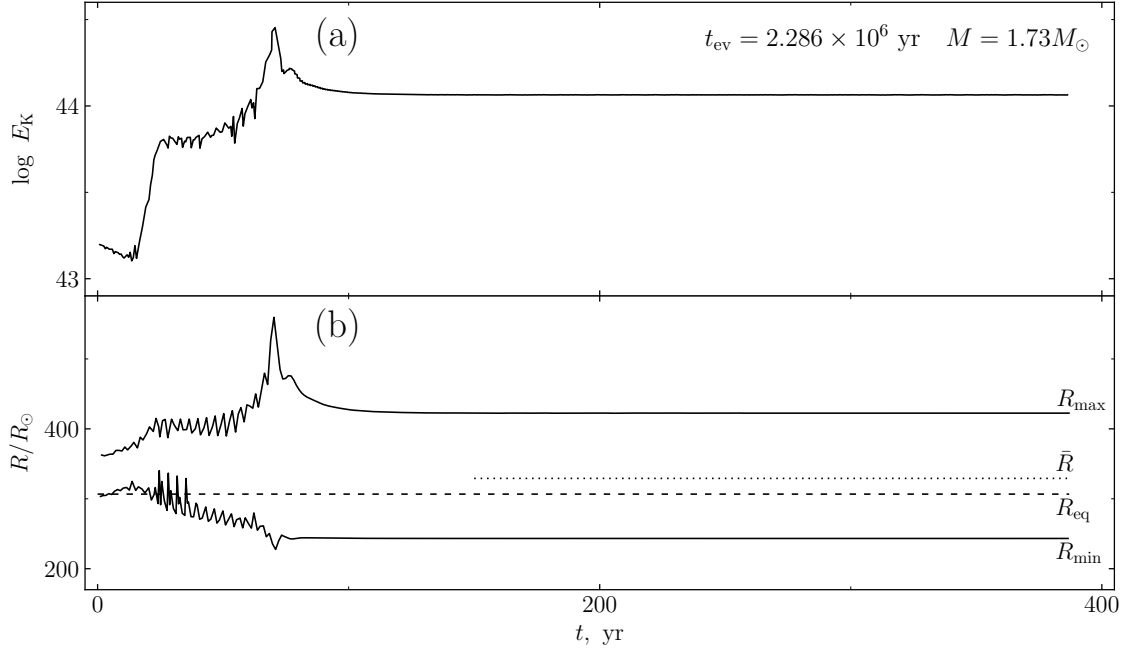


Figure 2. Variations of maximum values of the kinetic energy $E_{K,\max}$ (a) as well as maximum R_{\max} and minimum R_{\min} values of the outer boundary radius (b) of the hydrodynamic model computed for the evolutionary sequence $M_{\text{ZAMS}} = 2M_\odot$. The star age t_{ev} yr is set to zero at the first helium–shell flash. The stellar mass is $M = 1.73M_\odot$. The dashed and dotted lines show the radius of the equilibrium evolutionary model R_{eq} and the mean outer boundary radius of the hydrodynamic model \bar{R} .

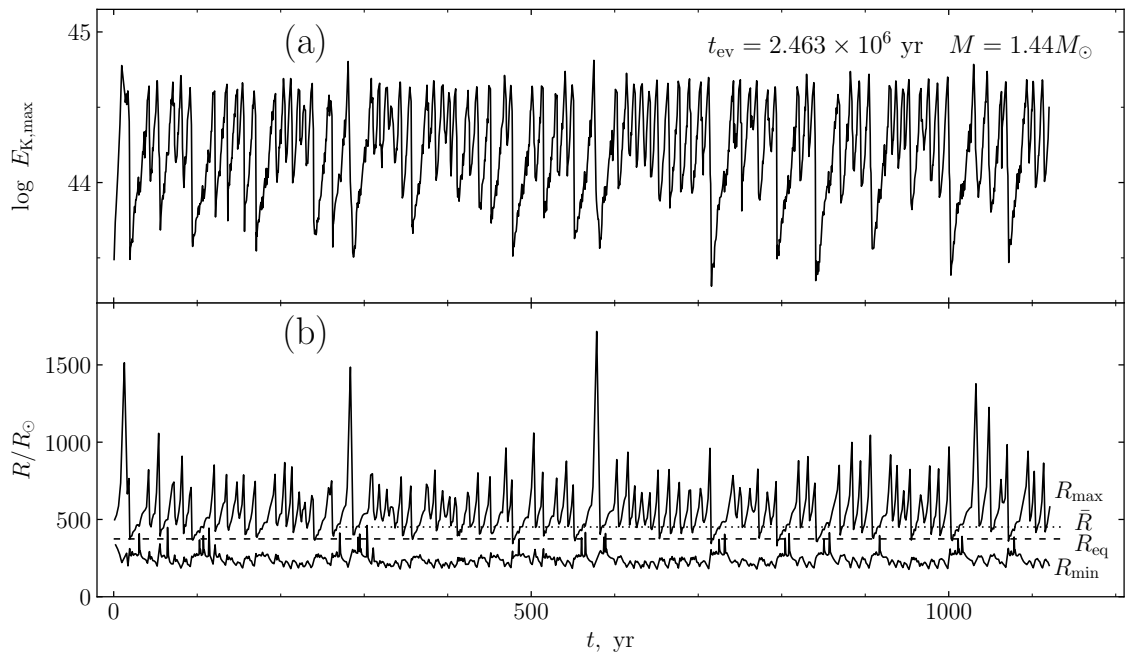


Figure 3. Same as Fig. 2 but for the hydrodynamic model of the AGB star with age $t_{\text{ev}} = 2.463 \times 10^6 \text{ yr}$ and the mass $M = 1.44 M_\odot$.

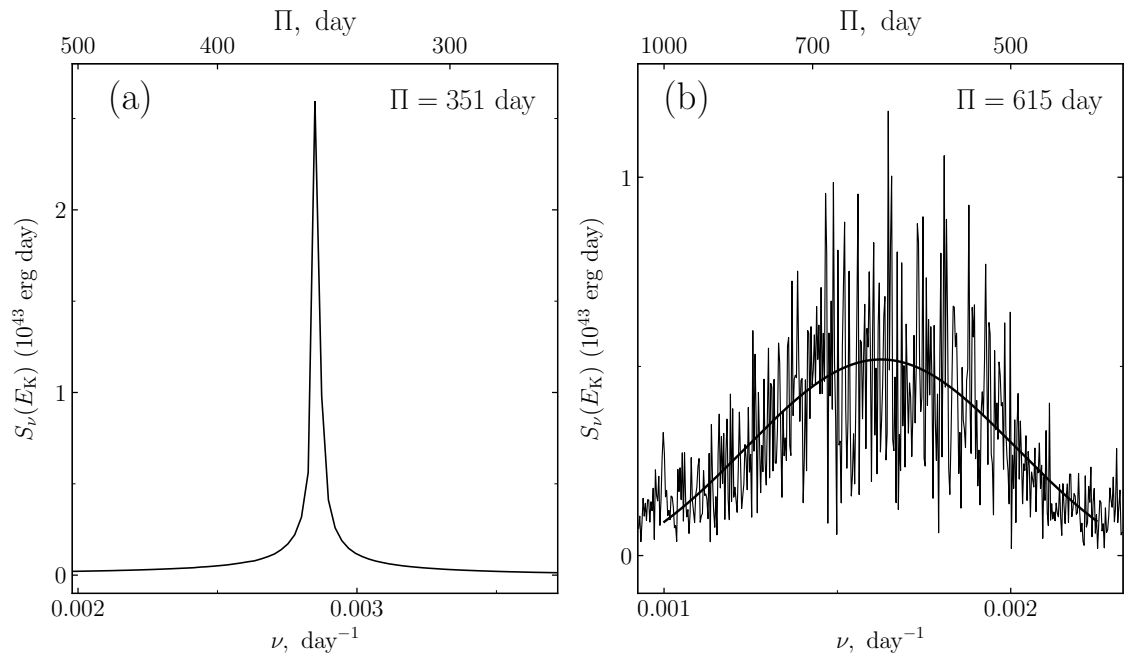


Figure 4. The spectral density of the kinetic energy of pulsation motions $S(E_K)$ for hydrodynamic models shown in Figs. 2 and 3. The least square fit of the spectral density by the gaussian function is shown by the thick solid line.

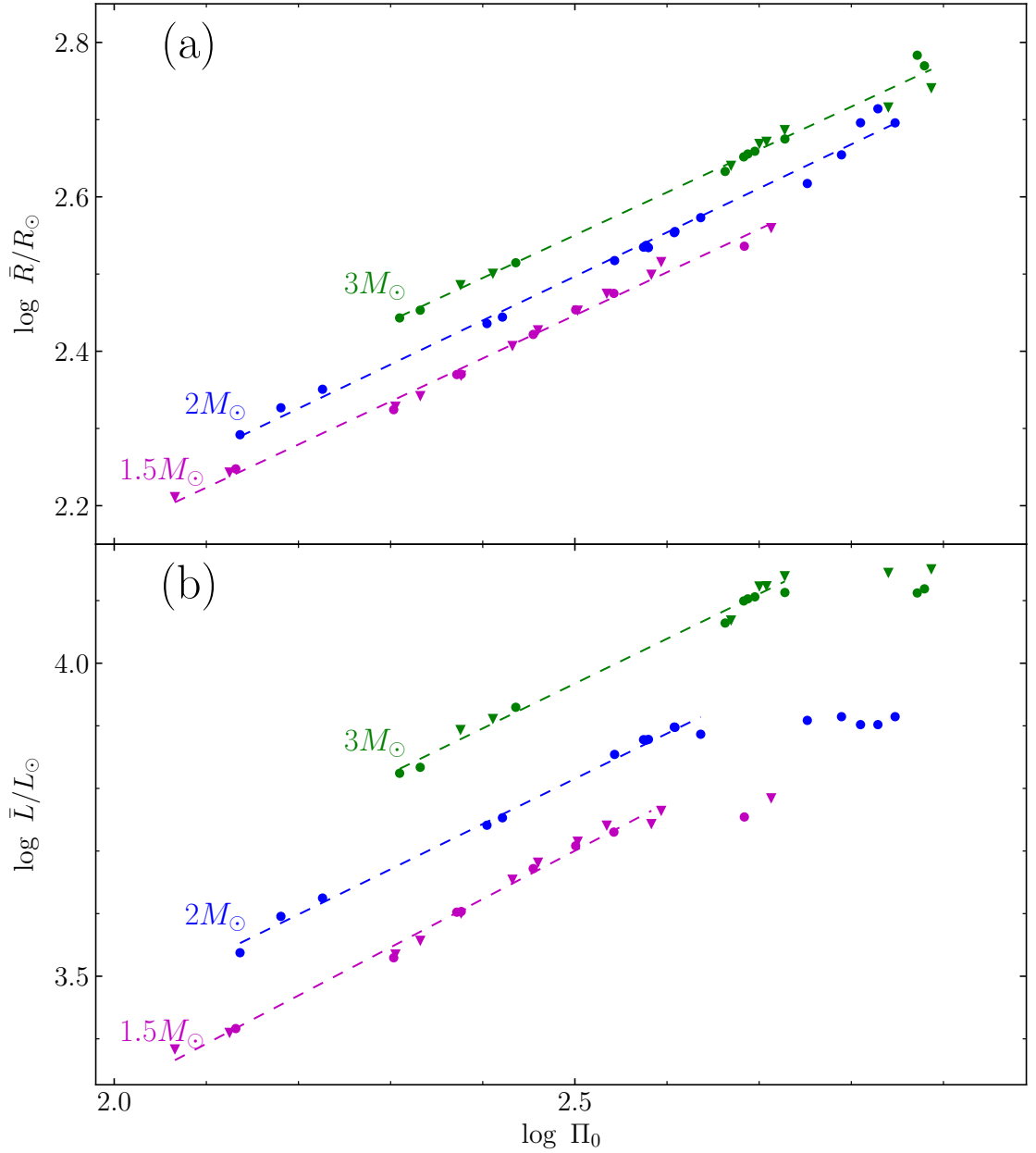


Figure 5. The period–radius (a) and period–luminosity (b) relations obtained from computations of hydrodynamic models of fundamental mode pulsators. The circles and triangles correspond to the models of evolutionary sequences computed with the mass loss rate parameters $\eta_B = 0.05$ and $\eta_B = 0.03$, respectively.

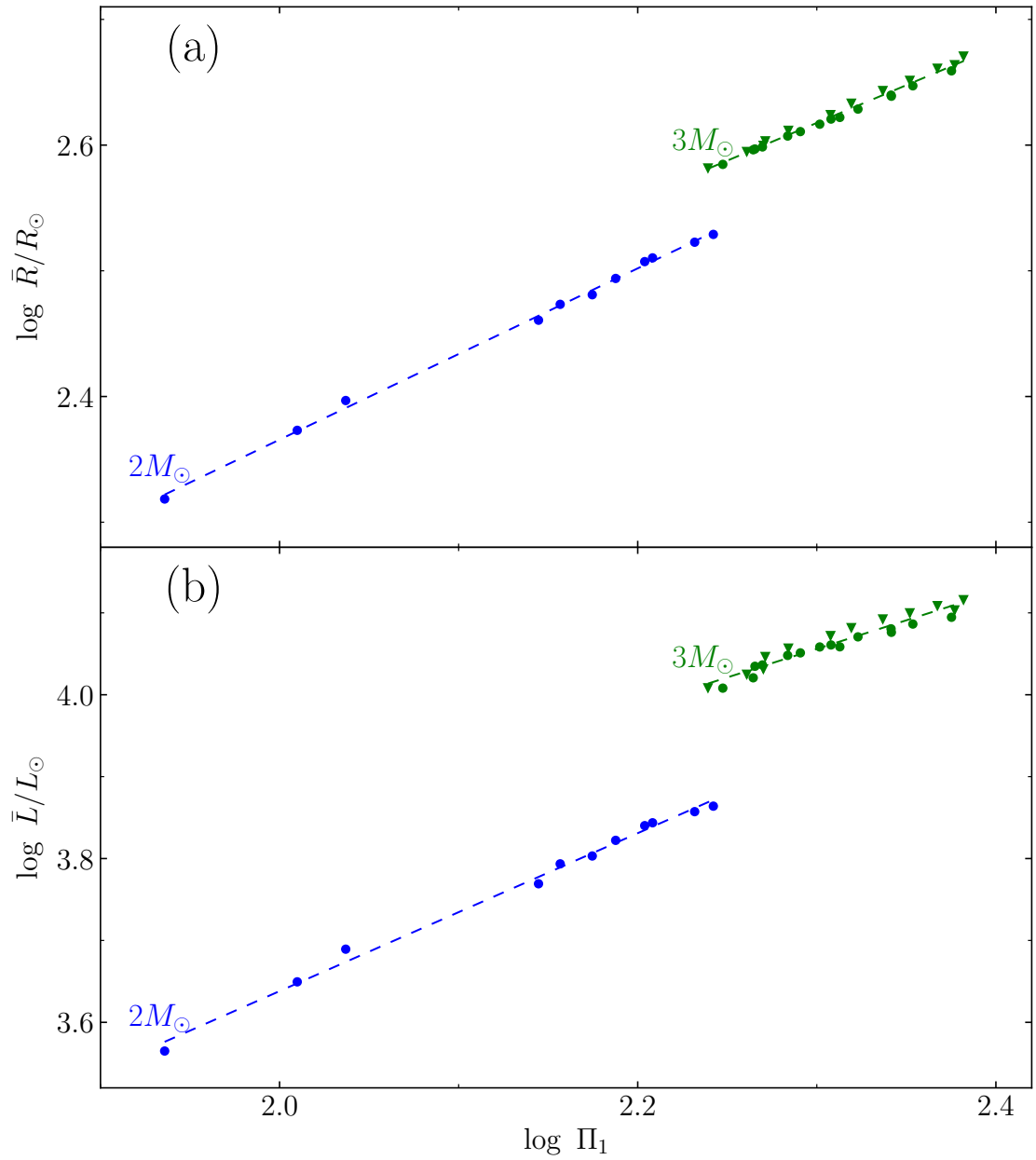


Figure 6. Same as in Fig. 5 but for hydrodynamic models of the first overtone pulsators.